THE JOURNAL OF PHYSICAL CHEMISTRY C
A JOURNAL OF THE AMERICAN CHEMICAL SOCIETY

pubs.acs.org/JPCC

Article

Atomic Structure and Valence State of Cobalt Nanocrystals on Carbon under Syngas Versus Hydrogen Reduction

Ofentse A. Makgae,* Tumelo N. Phaahlamohlaka, Benzhen Yao, Manfred E. Schuster, Thomas J. A. Slater, Peter P. Edwards, Neil J. Coville, Emanuela Liberti,* and Angus I. Kirkland

Cite This: *J. Phys. Chem. C* 2022, 126, 6325−6333

Read Online

ACCESS | Metrics & More | Article Recommendations | Supporting Information

ABSTRACT: The composition of the reducing gas in the activation of Co Fischer-Tropsch synthesis catalysts determines the nature of the catalytically active Co species. This study reports on the effect of H_2 versus syngas (H_2/CO = 2) on the reducibility of Co_3O_4 nanoparticles supported on hollow carbon spheres, using *ex situ* and *in situ* high-resolution aberration-corrected analytical electron microscopy. High-resolution images revealed twinned fcc Co particles encapsulated in carbon from syngas treatment while H_2-treated particles were mostly CoO. Moreover, the electron energy loss of the Co-$L_{3,2}$ and O-K edge fine structures show improved reducibility in syngas than in H_2 at 350 °C. The effect of high temperature on the reducibility of the Co_3O_4 nanoparticles is also explored. Carbon fiber encapsulation of twinned fcc Co particles observed during the syngas treatment provides sinter resistance at high temperatures. Both *ex situ* and *in situ* results indicate that syngas activation is efficient for obtaining highly reduced Co nanoparticles at lower temperatures.

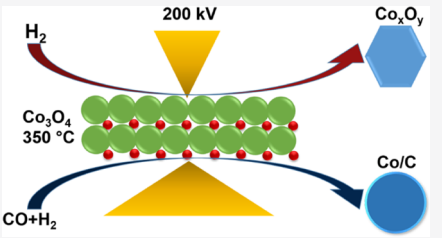

INTRODUCTION

Cobalt nanoparticles used in industrial Co Fischer−Tropsch synthesis (FTS) are active in their reduced metallic state.[1,2] Consequently, the production of active metallic Co is typically achieved by reducing spinel Co_3O_4 (or CoO) in the catalytic reactor before FTS. This is arguably one of the most critical steps in FTS as it determines the nature of the Co active sites produced.[2−12] However, depending on the reduction temperature, the composition of the reducing gas, the catalyst promoter, catalyst support, and particle size, Co_3O_4 may not entirely reduce to metallic Co. This results in a catalyst with mixed Co valence states, crystallographic phases, and surface terminations.[13]

Studies have shown that reducing Co_3O_4 under H_2, a direct syngas mixture, or sequential CO & H_2 treatment results in varying catalytic performance.[2,4−12] The difference is generally attributed to the Co crystallographic phases [i.e., hexagonal close-packed (hcp) vs cubic close-packed (ccp)] and valence states formed during reduction.[6,7,9,14−16] Temperature-programmed reduction (TPR) studies have shown that the reduction of Co_3O_4 with H_2 is a two-step process comprising the conversion of Co_3O_4 to CoO, followed by the conversion of CoO to Co.[17] In comparison, the reduction of Co_3O_4 with syngas proceeds through the formation of Co_2C, which decomposes to metallic hcp Co at lower temperatures (130−230 °C)[7,18−20] compared to the decomposition of CoO into ccp Co in H_2 at 500−600 °C.[17]

Conventionally, X-ray spectroscopic techniques have been used to determine the valence state of Co FT catalysts both *ex situ* and *in situ*.[9,13,21] However, these methods use bulk probes that lack the spatial resolution needed to determine the catalyst morphology, size, and local surface structure for correlation with the catalytic activity and selectivity.[22] Alternatively, electron energy loss spectroscopy[23] (EELS) can be used to obtain information about the valence state of Co,[24] in which variations in the Co valence state alter the L_3/L_2 peak intensity ratio of the Co-$L_{3,2}$ edge, the $L_{3,2}$ peak-to-peak energy separation, and the onset energy loss of the L_3 peak, as well as the O-K pre-peak.[25−27] These parameters can hence be used to measure the oxidation state of the catalyst quantitatively after reduction.

When carried out in conjunction with EELS, aberration-corrected scanning transmission electron microscopy (STEM) provides direct structural and chemical information at high spatial resolution.[23,28] Most studies of the pretreatment of Co catalysts for FTS using (S)TEM have focused on H_2 since it is well understood.[24,29−35] In contrast, there have been only limited studies on the activation of Co catalysts in syngas or comparisons of the effect of the activation gas composition. In addition, while many studies have explored the reduction behavior of Co catalysts on different inorganic oxide supports,[2,4−6,9−12] little work has been done to explore the role of C supports on the Co reduction process using H_2 or

Received: January 20, 2022
Revised: March 22, 2022
Published: April 4, 2022

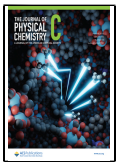

Downloaded via 80.43.152.180 on May 3, 2022 at 11:18:15 (UTC).
See https://pubs.acs.org/sharingguidelines for options on how to legitimately share published articles.

ACS Publications

© 2022 The Authors. Published by American Chemical Society

https://doi.org/10.1021/acs.jpcc.2c00482
J. Phys. Chem. C 2022, 126, 6325−6333

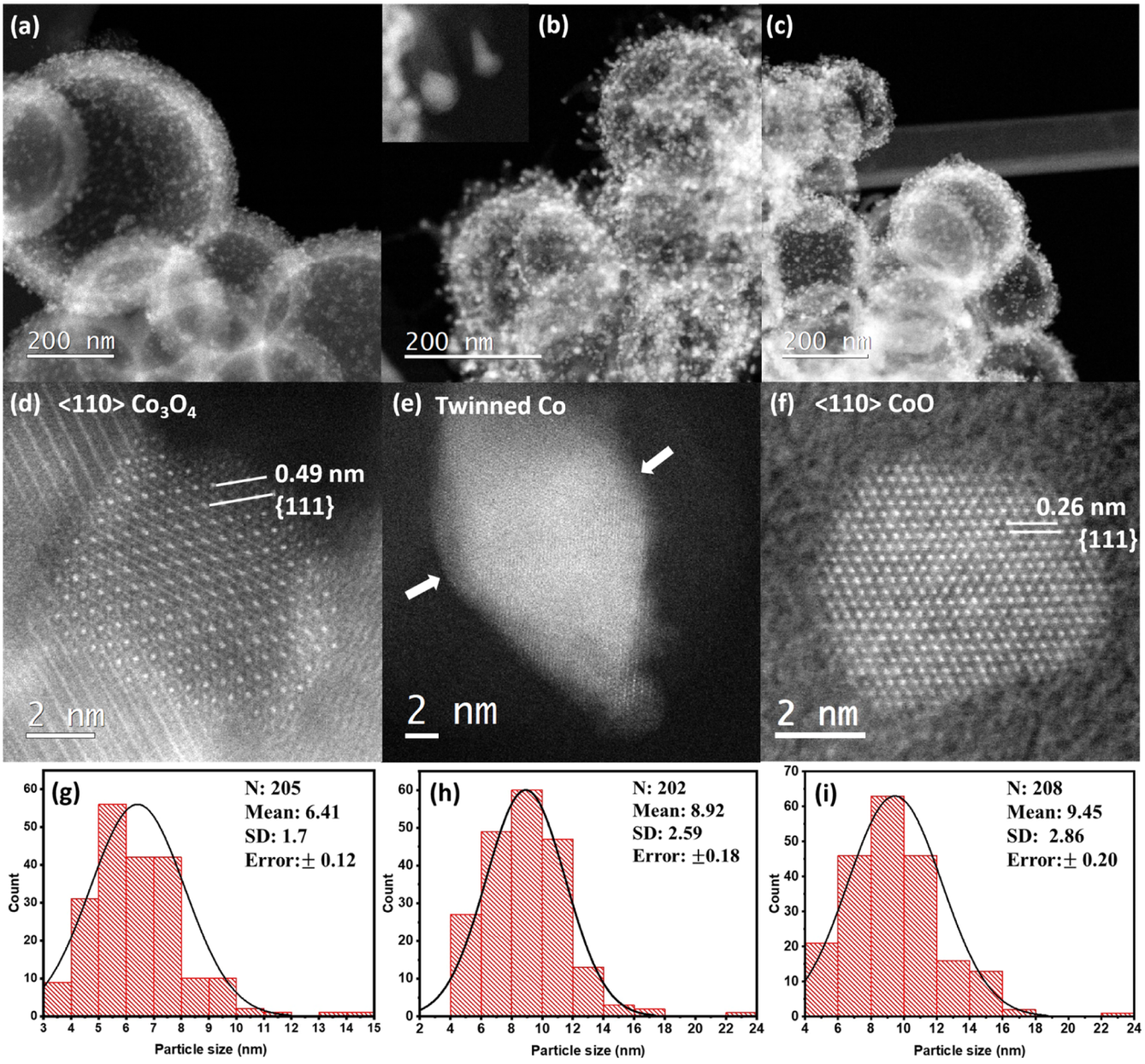

Figure 1. STEM−ADF images of the Co nanoparticles (a) before and after the *ex situ* reduction in (b) syngas (H_2/CO = 2) and (c) H_2 at 350 °C. (d−f) are the corresponding high-resolution STEM−ADF images of the as-prepared Co_3O_4, syngas-, and H_2-reduced nanoparticles. (g−i) are the average particle size distributions of the as-prepared Co_3O_4, syngas-, and H_2-reduced nanoparticles.

syngas. Unlike C supports, inorganic oxide supports, such as TiO_2, Al_2O_3, and SiO_2, generally have strong metal−support interaction, resulting in the formation of stable Co species (e.g., cobalt silicate) that can only be reduced at high temperatures.[36,37] Hence, studies of the effects of the catalyst activation method on the active metal catalyst's physicochemical properties require a more inert catalyst support that does not affect the properties and the reducibility of the catalyst.[38] This paper compares the atomic structure and valence states of Co supported on hollow carbon spheres (HCSs) reduced under H_2 and syngas (H_2/CO = 2) using both *ex situ* and *in situ* high-resolution aberration-corrected analytical electron microscopy.

EXPERIMENTAL SECTION

Synthesis of Co_3O_4 Supported on HCSs. In a typical procedure, Co_3O_4 nanoparticles (6.4 nm) were synthesized by a surfactant-free method using cobalt acetate as a precursor salt, benzyl alcohol as the solvent, and ammonia solution as the precipitating agent at 160 °C.[39] Subsequently, HCSs (diameter = 200 nm and shell thickness = 25 nm) were prepared by coating a spherical polystyrene (PSS) template with a resorcinol-formaldehyde (RF) polymer to form a composite (PSSs@RF).[40] Template removal and carbonization were performed in a one-step procedure inside a horizontal quartz tube by initially heating the composite under N_2 flow (50 mL/min) at 350 °C for 1 h to decompose and remove the polystyrene template, followed by thermal annealing of the HCSs at 600 °C for 2 h under N_2 atmosphere. Finally, the abovementioned presynthesized Co_3O_4 nanoparticles were

https://doi.org/10.1021/acs.jpcc.2c00482
J. Phys. Chem. C 2022, 126, 6325−6333

loaded on the surface of the HCSs using ethanol as the dispersing solvent in an ultrasonicator to prepare the precursor catalyst.

Reduction of Co_3O_4 Supported on HCSs. For *ex situ* analysis, the precursor (0.3 g, ca. 10% Co loading) was initially loaded in a quartz reactor and reduced in a tube furnace under a 100 mL/(min·g_{cat}) flow of 10% H_2/N_2 gas or syngas (H_2/CO/N_2 ~60/30/10 vol. %) at 350 °C at atmospheric pressure for 20 h. For this reaction, the effect of the H_2 content between 10% H_2 and syngas is insignificant because the volume of gas required to react completely with the loaded catalyst is infinitely smaller than the volume of gas supplied to the catalyst at 100 mL/min over the reaction duration. The reduced catalyst was subsequently stored in an argon gas-filled glovebox prior to analysis, and all specimens for electron microscopy were prepared in the glovebox. The specimens were mounted in a single tilt holder and transferred to the microscope. During this time, surface oxidation of the Co catalyst is expected. The catalysts were studied in a probe-corrected JEOL ARM200F at the electron Physical Science Imaging Centre (ePSIC) operated at 200 kV, equipped with a Gatan GIF Quantum 965 ER spectrometer.

For the *in situ* reduction, the same microscope was used with a DENS solutions Climate *in situ* nanoreactor gas supply system capable of real-time dynamic mixing of 3 gases over a temperature range from room temperature to 1300 °C. The gas supply system provided a 0.2 mL/min flow of gas at a pressure of 500 mbar for both H_2 (10 H_2/90 N_2) and syngas (10 H_2/5 CO/75 N_2) reduction. For both *ex situ* and *in situ* experiments, the syngas mixture was maintained at H_2/CO = 2. The temperature was ramped from room temperature to 150 °C under a N_2 flow to remove contaminants and then ramped to 350 °C at 10 °C/min under a reducing environment. The temperature was then held at 350 °C for 2 h for catalyst activation due to the impracticality of running a 20 h *in situ* gas-phase reaction in a microscope.

For both *ex situ* and *in situ* experiments, a probe current of 13 pA, convergence semiangle of 14 mrad, ADF inner- and outer-detector semiangles of 86.1−294.1 mrad, and a spectrometer collection semiangle of 39.6 mrad were used for the simultaneous acquisition of both EELS and ADF signals. Low-loss valence and core-loss spectra were acquired simultaneously using DualEELS with a 0.25 eV/ch dispersion and a pixel dwell time of 0.1 s. High-resolution ADF images were acquired using the same probe current at ADF inner- and outer-detector semiangles of 25.9−88.6 mrad, respectively. Additional STEM−EELS and ADF data were acquired on a probe-corrected JEOL ARM200F at the David Cockayne Centre for Electron Microscopy under the same conditions.

Data Processing. To extract the signal from the ionization edges in the core-loss region of the spectrum, the background subtraction was modeled as a power-law,[41,42] and the effect of multiple scattering was removed by Fourier-ratio deconvolution of the background-subtracted extracted core-loss edge signal to obtain a reliable quantification.[23,43,44] Elemental maps were constructed from the integrated intensities of the O-K and Co-$L_{3,2}$ ionization edges using ionization cross-sections calculated based on a Hartree−Slater model, as provided in Gatan Microscopy Suite (GMS) 3 software.[42,45,46] The values of the Co-$L_{3,2}$ intensities and energy losses were subsequently extracted and plotted from raw spectra using the ParticleSpy[47] python package (v 1.4) (https://github.com/ePSIC-DLS/ParticleSpy), using the fitting functionality of the Hyperspy[48] python package (v 1.6.0). This automated curve fitting in python to extract the data from raw spectra eliminates human error arising from inconsistent background subtraction and peak intensity measurements. However, accurate peak fitting and data measurement using this script depend on the quality of the raw data (Figure S1, Supporting Information) and, in particular, noisy data led to less accurate peak fitting because it is difficult to distinguish signal from noise (Figure S1b), resulting in outliers in the scatter plots.

RESULTS AND DISCUSSION

The integrity of the HCS support may be compromised during reduction with H_2 by removing C from the support to form methane.[49] This may result in the depletion of the support and subsequent particle sintering. Hence, it is essential to analyze the overall morphology (mainly the shape of the carbon support) post reduction. Figure 1a−i shows low magnification and high-resolution STEM−ADF images, together with the average particle size distributions, of the as-prepared Co_3O_4 and *ex situ* syngas- and H_2-reduced HCS-supported nanoparticles. The structure (morphology) of the supporting spheres remains intact after 20 h of reduction at 350 °C.

In contrast to the Co_3O_4 precursor and the H_2-reduced nanoparticles, the syngas-reduced nanoparticles (Figure 1b) are partially encapsulated by carbon nanofibers (CNFs) formed by the CO disproportionation, and the Co-catalyzed nucleation and growth of the atomic C from CO dissociation (see Figure S2, Supporting Information).[35,50,51] It has been suggested that the CO dissociation could lead to a deactivation of active catalytic sites through surface coverage by graphitic C and possible Co_2C formation.[50−52] However, it has also been proposed that the presence of H_2 in syngas (for H_2/CO > 1) promotes the gasification of excess C as methane.[35,52] This creates a porous C shell through which the Co active sites are accessible to the reactants.[5−9] Also, the formation of highly graphitic carbon at 350 °C is unlikely.

The as-prepared Co_3O_4, *ex situ* syngas-, and H_2-reduced nanoparticles have average particle size distributions of 6.41 ± 0.12, 8.92 ± 0.18, and 9.45 ± 0.20 nm, respectively (Figure 1g−i). The observed increase in the average particle size distributions of the reduced nanoparticles compared to the as-prepared Co_3O_4 is attributed to particle coalescence/crystal merging during reduction at 350 °C, inevitably leading to the formation of twin boundaries[53] in syngas-reduced ccp Co nanoparticles, as seen in Figure 1e. Notably, syngas-reduced nanoparticles have a smaller average size distribution than H_2-reduced nanoparticles. We believe the smaller average particle size distribution in syngas compared to H_2-reduced nanoparticles is owed to the sinter-resistance provided by the CNFs, which prevents excessive particle coalescence.

The nanoparticles of the as-prepared Co_3O_4 (Figure 1d) exhibit a faceted cubic morphology projected in a ⟨110⟩ zone axis with a 0.49 nm interplanar spacing between the {111} planes consistent with a *normal* spinel crystal structure and particle shape obtained in the applied synthesis[39] strategy. The morphologies of the syngas- (Figure 1e) and H_2-(Figure 1f) reduced nanoparticles have a pseudospherical shape due to loss of faceting under the elevated temperature reduction commonly observed in the thermal treatment of nanoparticles.[54] The atomic structure of the H_2- and syngas-reduced nanoparticles is discussed in detail later.

In addition to changes in morphology, the oxidation state of Co also changes during the reduction process. The Co-

https://doi.org/10.1021/acs.jpcc.2c00482
J. Phys. Chem. C 2022, 126, 6325−6333

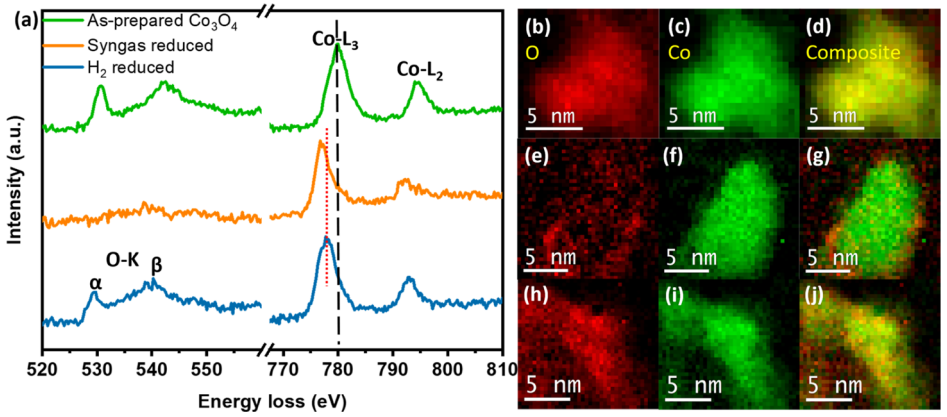

Figure 2. EELS spectra of the as-prepared Co_3O_4 (green), syngas- (orange), and H_2- (blue) *ex situ* reduced nanoparticles at 350 °C. The black dashed line shows the Co-L_3 edge energy difference between the as-prepared Co_3O_4 and reduced nanoparticles, while the red dotted line shows the energy difference between the syngas- and H_2-reduced particles. EELS elemental maps of (b–d) as-prepared, (e–g) syngas-reduced, and (h–j) H_2-reduced Co_3O_4 nanoparticles. Spectrum images were acquired using a 0.25 eV/ch dispersion with a pixel dwell time of 0.1 s and pixel size of 0.52, 0.4, and 0.42 nm/pix, respectively. The red and green regions represent the integrated O-K edge and Co-$L_{3,2}$ edge signals.

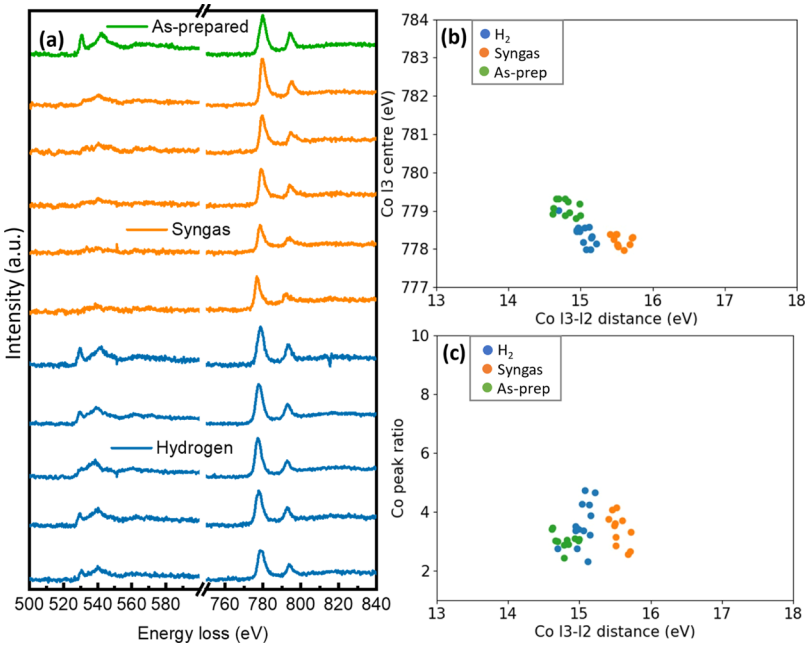

Figure 3. (a) EELS spectra of the as-prepared Co_3O_4 (green spectrum), 350 °C *ex situ* syngas- (orange spectra), and H_2- (blue spectra) reduced nanoparticles. (b,c) Scatter plots of the Co L_3/L_2 intensity ratio vs Co L_3–L_2 distance and Co-L_3 position vs Co L_3–L_2 distance, respectively. Each spectrum was recorded from a single nanoparticle. Spectrum images were acquired using the same conditions as in Figure 2.

oxidation state changes as a function of the reducing gas composition were investigated using STEM–EELS. Figure 2a–j compares the EELS spectra and elemental maps of single particles of the as-prepared Co_3O_4, and the syngas- and H_2--reduced nanoparticles. The as-prepared Co_3O_4 EELS spectrum (green in Figure 2a) exhibits the typical O-K edge and Co-$L_{3,2}$ edge fine structure expected for spinel cobalt oxide materials.[33,55] In Figure 2a, peak α at ∼530 eV corresponds to electronic transitions from the O 1s states to hybridized O 2p–Co 3d states. Peak β at ∼543 eV is typically a broad peak due to an unresolved shoulder and has been attributed to transitions from the O 1s state to O 2p–Co 3d and O 2p–Co 3sp states.[27] The Co-$L_{3,2}$ edge-fine structure consists of two white lines, the Co-L_3 peak (∼778 eV) and the Co-L_2 peak (∼794 eV), corresponding to transitions from $2p_{3/2}$ and $2p_{1/2}$ to unoccupied 3d states.[25]

Visual evaluation of all the three EELS spectra in Figure 2a show that the position of the Co-L_3 edge is shifted to a lower energy loss by at least ∼3 eV in the reduced nanoparticles' spectra compared to the Co_3O_4 spectrum. Also, a decrease in the O-K edge α peak's relative intensity is observed in the reduced nanoparticles' O-K edge fine structure (Figure 2a) compared to the Co_3O_4. These observations are indicative of a decrease in the oxidation state of Co.[25,27]

However, the differences in the features of the O-K edge fine structure (Figure 2a) of the two methods (H_2 and syngas) indicate varying degrees of reduction. Therefore, additional spectra were collected for comparison between *ex situ* syngas- and H_2-reduced nanoparticles at 350 °C, with the as-prepared Co_3O_4 as a reference, and these are shown in Figure 3a–c. In Figure 3a, features in the O-K edge fine structure (∼530–545 eV) from the H_2-reduced nanoparticles (blue spectra) are

https://doi.org/10.1021/acs.jpcc.2c00482
J. Phys. Chem. C 2022, 126, 6325–6333

more clearly defined, with a resolved α peak (~530 eV) and a relatively intense β peak (~543 eV) compared to spectra from the syngas-reduced nanoparticles (orange spectra). Moreover, the absence of the O-K edge α peak (~530 eV) and the diminished O-K edge signal in the syngas-reduced nanoparticles' spectra suggest the Co here is in a near metallic state compared to the H_2-reduced nanoparticles. This is also consistent with the more intense Co signal (green) in the elemental map from a syngas-reduced nanoparticle (Figure 2g), compared to a more diffuse Co signal in the elemental map of a H_2-reduced nanoparticle (Figure 2j).

The Co L_3/L_2 peak intensity ratio, Co L_3-L_2 peak-to-peak energy separation, and the Co/L_3 peak position values were plotted from the spectra (raw data) of the as-prepared Co_3O_4, syngas-, and H_2-reduced HCS-supported nanoparticles for semiquantitative comparisons using the ParticleSpy package (Figure 3b,c). These experimental values were also compared to EELS spectra from standard Co samples (Figure S3 & Table 1) with known oxidation states. However, a metallic Co standard sample was not measured since Co readily oxidizes in air and is unavailable as a metallic commercial standard. Hence, in this instance, data were compared with reported values for metallic Co reduced and measured *in situ*.[24]

Table 1. Data Obtained from the EELS Spectra of Co Standards with Known Oxidation States in Figure S3

spectra	L_3/L_2	L_3-L_2 (eV)	Co-L_3 (eV)
Co^{3+}	2.29	14.5	780.3
Co^{3+}/Co^{2+} (spinel)	2.40	14.75	779.6
Co^{2+}	4.51	15.75	778.4

The clear separation in the distribution of the data points in the scatter plots (Figure 3b,c) indicates that the as-prepared Co_3O_4, syngas-, and H_2-reduced nanoparticles have different Co-oxidation states. Specifically, the average Co L_3-L_2 peak-to-peak separation for the H_2-reduced nanoparticles' EELS spectra (15.07 ± 0.02 eV) is smaller than the Co L_3-L_2 peak-to-peak separation (15.7 ± 0.03 eV) for syngas-reduced nanoparticles (Figure 3b,c). Moreover, the average Co L_3-L_2 peak-to-peak separation of the as-prepared Co_3O_4 (14.78 ± 0.05 eV) EELS spectra is smaller than in both the syngas- and H_2-reduced nanoparticles. The average Co L_3-L_2 peak-to-peak separation of the H_2-reduced nanoparticles and the as-prepared Co_3O_4 is consistent with standard Co^{2+} (15.75) and spinel oxide (14.75), respectively (Table 1). In addition, the average Co-L_3 peak position is slightly shifted to lower energy losses for the syngas (778.0 ± 0.07 eV) compared to the H_2- (778.3 ± 0.06 eV) reduced nanoparticles and the as-prepared Co_3O_4 (779.1 ± 0.06 eV) (Figure 3b). The average Co-L_3 peak positions for H_2 and the as-prepared Co_3O_4 are comparable to the standard Co^{2+} and spinel cobalt oxide, respectively (Table 1). It has been reported[25,56] that this increase in the Co L_3-L_2 peak-to-peak separation, accompanied by a shift in the Co-L_3 edge to lower energy losses, indicates an increase in the number of d electrons in a more highly reduced state.

The syngas reduced nanoparticles' average Co-L_3/L_2 intensity ratio (3.4 ± 0.16) is comparable to the ratio (~3.15) reported for *in situ* reduced metallic Co,[24] indicating a higher degree of Co^0, which is in agreement with the elemental map (Figure 2g). In contrast, the Co-L_3/L_2 intensity ratio of the standard CoO sample (~4.51) in Table 1 was comparable to that of the H_2 reduced nanoparticles (3.9 ± 0.18), indicating that the particles are mostly Co^{2+}. The difference (~0.4) in the measured average Co L_3/L_2 ratio of the samples from the standard Co L_3/L_2 ratios likely results from mixed Co-oxidation states due to surface reoxidation of the reduced nanoparticles in air. Nevertheless, our preliminary results (Figure S4, Supporting Information) on *in situ* STEM–EELS and ADF, in the absence of air surface reoxidation, show that syngas achieves a higher degree of Co reduction than H_2.

In addition to EELS, high-resolution STEM–ADF imaging was used to investigate the differences in the atomic structure associated with the observed differences in Co-oxidation states in the syngas- and H_2-reduced nanoparticles. Figure 4a–e

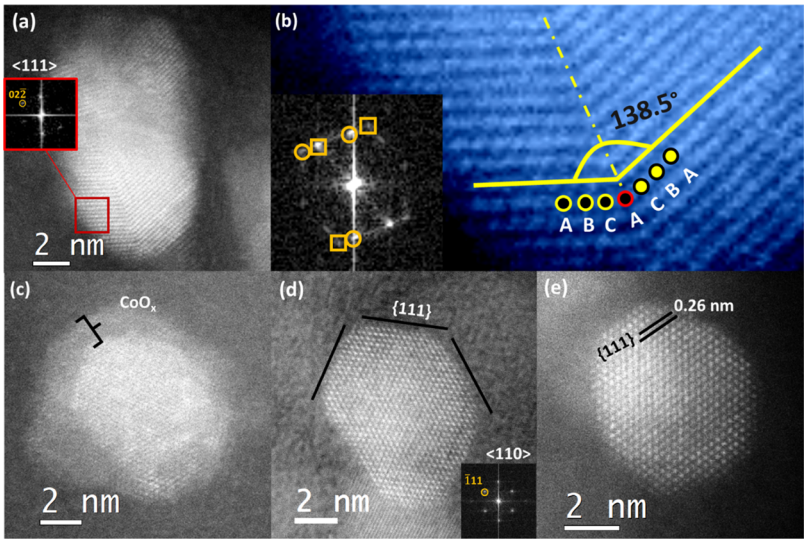

Figure 4. High-resolution STEM–ADF images of *ex situ* (a–c) 350 °C syngas- and (d,e) H_2-reduced nanoparticles. (b) Magnified, false-color STEM–ADF image of the twin boundary of the particle in (a) showing the 138.5° boundary angle and the stacking sequence with reversed {111} planes. Power spectra calculated from the images in (a,b,d) are insets. The power spectrum inset in (b) corresponds to ⟨111⟩ ccp Co with doubled {022} reflections (labeled in a yellow box and circle) resulting from two overlapping single crystals of ⟨111⟩ ccp Co mirrored at a 138.5° twin boundary angle. The power spectrum inset in (d) corresponds to a ⟨110⟩ projection of the CoO rocksalt structure.

https://doi.org/10.1021/acs.jpcc.2c00482
J. Phys. Chem. C 2022, 126, 6325–6333

shows high-resolution STEM−ADF images of syngas- (a−c) and H_2- (d,e) reduced nanoparticles. Some of the nanoparticles reduced at 350 °C in syngas show twinning on {111} planes (Figure 4a), while some show a core−shell structure, with a metallic Co core and a metal oxide shell (Figure 4c), consistent with surface reoxidation of metallic Co. As mentioned earlier, the coalescence of particles can also lead to the formation of twin boundaries via crystal merging at a common facet.[53] We also note that twinning in ccp metals *via* the stacking fault in the {111} planes is also a common structural configuration in the thermally annealed ccp metals in an attempt to balance the internal strain at a given particle volume and the surface energy during volume change from Co_3O_4 to Co at 350 °C.[57,58] Here, twinning from both crystal merging (evidenced by the increased average particle size distribution) and temperature-induced defect formation ({111} stacking fault) to stabilize crystal energetics and strain during phase change from Co_3O_4 to Co at 350 °C cannot be ruled out. The structure of such a twin boundary follows a reversed ccp {111} stacking sequence (ABCACBA) (Figure 4b). The doubled {022} reflections (labeled in a yellow box and circle in Figure 4b inset) in the power spectrum result from two merged single crystals of ⟨111⟩ ccp Co mirrored at 138.5°, corresponding to the twin boundary angle (Figure 4b). Previous reports[57,58] indicate that these are typical features of {111}-type twin boundaries found in ccp transition metals.

In contrast, nanoparticles reduced in H_2 at 350 °C showed faceted hexagonal particles (Figure 4d,e). The power spectrum (Figure 4d inset) and the measured 0.26 nm interatomic spacing are consistent with {111} planes of CoO in a ⟨110⟩ orientation, and the particle morphology corresponds to CoO particles enclosed by {111} facets (Figure 4d). This is consistent with our EELS data which showed that syngas reduction produces a majority of metallic Co nanoparticles, while H_2 produced particles with a majority of the Co in the 2+ oxidation state (see Figure S5 & S6, Supporting Information). There were no twin boundaries observed in H_2-reduced nanoparticles. Twin boundaries are important defects in catalysis since they typically have higher adsorption energies in comparison to flat facets and are stable during chemical reactions.[59,60] Thus, the presence of such defects may also explain the varying catalytic performance of syngas-activated catalysts over H_2-activated catalysts in FTS.

In the second set of experiments, the temperature was increased to 600 °C to investigate the effect of temperature on reducing HCS-supported Co_3O_4 nanoparticles under H_2 versus syngas. Temperatures above 600 °C permit the conversion of CoO to Co^0, as according to TPR,[17] this temperature is required to obtain metallic Co in H_2. Indeed, both the H_2- and syngas-reduced nanoparticles exhibit atomic structure consistent with Co ccp (Figure 5a−d). Specifically, Figure 5a,c show a ⟨110⟩ ccp metallic Co structure, confirmed by the power spectra (insets) and a measured 0.21 nm interplanar spacing between the {111} planes. This is consistent with EELS data from the 600 °C reduced nanoparticles, which shows the presence of metallic Co (Figure S7, Supporting Information). High-resolution images show the presence of stacking faults on {111} planes (Figure 5c) in the H_2-reduced nanoparticles as commonly observed in ccp metal particles after high-temperature treatment.[57] Therefore, to achieve a complete reduction of Co_3O_4 (in the absence of a promoter) under H_2, the HCS-supported nanoparticles must be reduced at high temperatures.

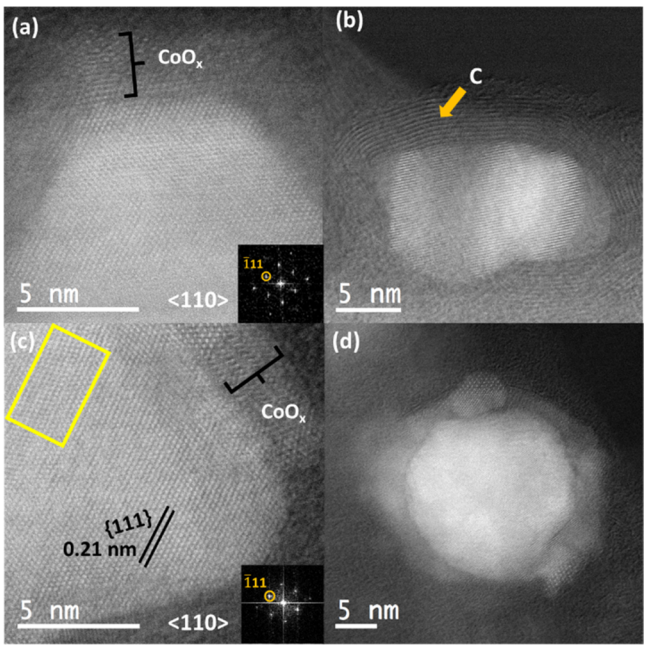

Figure 5. High-resolution STEM−ADF images of 600 °C *ex situ* (a,b) syngas- and (c,d) H_2-reduced Co nanoparticles. Insets in (a,c) are calculated power spectra corresponding to ⟨110⟩ ccp Co. The orange arrow in (b) shows the surface coverage by graphitic carbon.

However, high temperature resulted in severe sintering of the nanoparticles reduced in H_2 compared to syngas (Supporting Information Figure S8). The sinter-resistance in syngas-reduced nanoparticles is attributed to the encapsulation of nanoparticles with graphitic C from CO disproportionation, which prevents the coalescence of the nanoparticles at high temperatures, as shown by the orange arrow in Figure 5b. In contrast, a C shell is not observed in the H_2-reduced nanoparticles, Figure 5d. As discussed earlier, the nanoparticle surface coverage by graphitic C could lead to a deactivation of active catalytic sites and possible Co_2C formation.[50−52]

It is essential to reconcile the above differences in Co-oxidation states and crystal structure of H_2- and syngas-reduced nanoparticles with the reactions of these gases with Co_3O_4. The reactions of syngas with Co_3O_4 (see Table S1, Supporting Information) that yields metallic Co are energetically favored over the corresponding H_2 reactions with Co_3O_4. Significantly, the presence of CO in syngas seems to play a critical role in the conversion of Co_3O_4 to metallic Co through the formation of Co_2C from CO (eq 5 Table S1), which spontaneously decomposes into metallic Co in H_2 (eq 6 Table S1) at temperatures as low as 150 °C.[6,7,18,19,61]

In this work, the presence of carbide phases is not ruled out. However, if present, it is not expected to be in significant amounts as the H-rich syngas promotes the carbide decomposition to metallic Co, which is thermodynamically preferred (see Table S1, Supporting Information). Also, our high-resolution STEM−ADF data show crystallography consistent with ccp Co without observing the typical Co_2C (002) 0.217 nm lattice fringe commonly reported in the literature.[62] Moreover, the presence of the C support renders the analysis of the EELS C-K edge unreliable since it contributes to an overlapping signal. A recent study did suggest that an analysis of the peak broadening of the Co-L_3 edge could be used to estimate the presence of Co_2C.[63]

https://doi.org/10.1021/acs.jpcc.2c00482
J. Phys. Chem. C 2022, 126, 6325−6333

However, the similarity of the Co^{2+} oxidation state in both CoO and Co_2C renders the analysis of the Co-$L_{3,2}$ fine structure for the presence of Co_2C problematic.

The H_2-CO synergistic effect is not found in H_2 activation, and hence, better reducibility is achieved with syngas than H_2. These findings agree with previous studies, showing that the reduction of Co_3O_4 in H_2 does not achieve complete reduction at 350 °C.[7,29] Hence, the presence of CO in a syngas mixture is crucial to achieving complete Co_3O_4 reduction at 350 °C.

CONCLUSIONS

We have shown that the reduction of HCS-supported Co_3O_4 nanoparticles under either H_2 or syngas directly affects the physicochemical properties of the reduced nanoparticles. The presented data suggest that syngas achieves a higher reduction at an industrially relevant FT reduction temperature (350 °C) than H_2 on carbon supports. Our observations have revealed that at 350 °C, *ex situ* H_2 activation produced mainly CoO catalyst particles bounded by {111} facets. In contrast, activation in syngas produced twinned fcc Co particles encapsulated in carbon fibers and core−shell particles, with a metallic Co core and a CoO shell. Increasing the activation temperature to 600 °C helped drive the complete reduction of CoO to active metallic Co in H_2. However, significant particle sintering was observed in H_2-reduced nanoparticles. In contrast, carbon encapsulation in the syngas-activated catalyst provided sintering resistance during high-temperature activation. Overall, we have shown that syngas activation is the most effective method to obtain sintering-resistant metallic Co nanoparticles at lower temperatures on these types of carbon supports.

ASSOCIATED CONTENT

Supporting Information

The Supporting Information is available free of charge at https://pubs.acs.org/doi/10.1021/acs.jpcc.2c00482.

Effect of S/N on the peak fitting; EELS data for 600 °C *ex situ* and 350 °C *in situ* reduced nanoparticles; particle size of the 600 °C reduced nanoparticles; elemental maps of the 350 °C reduced nanoparticles; and considerations of beam effects (PDF)

AUTHOR INFORMATION

Corresponding Authors

Ofentse A. Makgae − *National Centre for High-Resolution Electron Microscopy (nCHREM), Centre for Analysis and Synthesis, Lund University, Lund 221 00, Sweden; Department of Materials, University of Oxford, Oxford OX1 3PH, U.K.;* orcid.org/0000-0002-1664-9416; Email: ofentse.makgae@chem.lu.se

Emanuela Liberti − *Department of Materials, University of Oxford, Oxford OX1 3PH, U.K.; Electron Physical Science Imaging Centre (ePSIC), Diamond Light Source Ltd., Didcot OX11 0DE, U.K.*; Email: emanuela.liberti@materials.ox.ac.uk

Authors

Tumelo N. Phaahlamohlaka − *Molecular Sciences Institute, School of Chemistry and DSI-NRF Centre of Excellence in Catalysis, University of the Witwatersrand, Johannesburg 2050, South Africa*

Benzhen Yao − *King Abdulaziz City for Science and Technology (KACST)—Oxford Centre of Excellence in Petrochemicals, Inorganic Chemistry Laboratory, Department of Chemistry, University of Oxford, Oxford OX1 3QR, U.K.;* orcid.org/0000-0002-4117-0538

Manfred E. Schuster − *Johnson Matthey Technology Centre, Reading RG4 9NH, U.K.*

Thomas J. A. Slater − *Cardiff Catalysis Institute, School of Chemistry, Cardiff University, Cardiff CF10 3AT, U.K.; Electron Physical Science Imaging Centre (ePSIC), Diamond Light Source Ltd., Didcot OX11 0DE, U.K.;* orcid.org/0000-0003-0372-1551

Peter P. Edwards − *King Abdulaziz City for Science and Technology (KACST)—Oxford Centre of Excellence in Petrochemicals, Inorganic Chemistry Laboratory, Department of Chemistry, University of Oxford, Oxford OX1 3QR, U.K.;* orcid.org/0000-0001-7340-4856

Neil J. Coville − *Molecular Sciences Institute, School of Chemistry and DSI-NRF Centre of Excellence in Catalysis, University of the Witwatersrand, Johannesburg 2050, South Africa;* orcid.org/0000-0003-1174-5078

Angus I. Kirkland − *Department of Materials, University of Oxford, Oxford OX1 3PH, U.K.; Electron Physical Science Imaging Centre (ePSIC), Diamond Light Source Ltd., Didcot OX11 0DE, U.K.*

Complete contact information is available at: https://pubs.acs.org/10.1021/acs.jpcc.2c00482

Author Contributions

The manuscript was written through the contributions of all authors. All authors have approved the final version of the manuscript.

Notes

The authors declare no competing financial interest.

ACKNOWLEDGMENTS

The authors would like to thank the David Cockayne Centre for Electron Microscopy for the South of England Analytical Electron Microscope (EPSRC grant, EP/K040375/1), the Johnson Matthey Technology Centre, and the Diamond Light Source for access and support in the use of the electron Physical Science Imaging Centre (ePSIC) (Instrument E01 and proposal number EM20403) that contributed to the results presented here. The DSI-NRF Centre of Excellence in Catalysis (South Africa) is thanked for financial assistance.

REFERENCES

(1) Khodakov, A. Y.; Chu, W.; Fongarland, P. Advances in the Development of Novel Cobalt Fischer−Tropsch Catalysts for Synthesis of Long-Chain Hydrocarbons and Clean Fuels. *Chem. Rev.* **2007**, *107*, 1692−1744.

(2) Pan, Z.; Parvari, M.; Bukur, D. B. Fischer−Tropsch Synthesis on Co/ZnO − Two Step Activation Procedure for Improved Performance. *Appl. Catal., A* **2014**, *480*, 79−85.

(3) Mitchell, R. W.; Lloyd, D. C.; van de Water, L. G. A.; Ellis, P. R.; Metcalfe, K. A.; Sibbald, C.; Davies, L. H.; Enache, D. I.; Kelly, G. J.; Boyes, E. D.; Gai, P. L. Effect of Pretreatment Method on the Nanostructure and Performance of Supported Co Catalysts in Fischer−Tropsch Synthesis. *ACS Catal.* **2018**, *8*, 8816−8829.

(4) Pan, Z.; Parvari, M.; Bukur, D. B. Fischer−Tropsch Synthesis on Co/Al_2O_3 Catalyst: Effect of Pretreatment Procedure. *Top. Catal.* **2014**, *57*, 470−478.

(5) de la Peña O'Shea, V. A.; Campos-Martín, J. M.; Fierro, J. L. G. Strong Enhancement of the Fischer−Tropsch Synthesis on a Co/SiO_2

Catalyst Activate in Syngas Mixture. *Catal. Commun.* **2004**, *5*, 635−638.
(6) Gnanamani, M. K.; Jacobs, G.; Shafer, W. D.; Davis, B. H. Fischer−Tropsch Synthesis: Activity of Metallic Phases of Cobalt Supported on Silica. *Catal. Today* **2013**, *215*, 13−17.
(7) Ducreux, O.; Rebours, B.; Lynch, J.; Roy-Auberger, M.; Bazin, D. Microstructure of Supported Cobalt Fischer-Tropsch Catalysts. *Oil Gas Sci. Technol.* **2009**, *64*, 49−62.
(8) Dehghan, R.; Hansen, T. W.; Wagner, J. B.; Holmen, A.; Rytter, E.; Borg, Ø.; Walmsley, J. C. In-Situ Reduction of Promoted Cobalt Oxide Supported on Alumina by Environmental Transmission Electron Microscopy. *Catal. Lett.* **2011**, *141*, 754−761.
(9) de la Peña O'Shea, V. A.; Homs, N.; Fierro, J. L. G.; Ramírez de la Piscina, P. Structural Changes and Activation Treatment in a Co/SiO_2 Catalyst for Fischer−Tropsch Synthesis. *Catal. Today* **2006**, *114*, 422−427.
(10) Gnanamani, M. K.; Jacobs, G.; Keogh, R. A.; Shafer, W. D.; Sparks, D. E.; Hopps, S. D.; Thomas, G. A.; Davis, B. H. Fischer-Tropsch Synthesis: Effect of Pretreatment Conditions of Cobalt on Activity and Selectivity for Hydrogenation of Carbon Dioxide. *Appl. Catal., A* **2015**, *499*, 39−46.
(11) Dai, X.; Yu, C. Effects of Pretreatment and Reduction on the Co/Al_2O_3 Catalyst for CO Hydrogenation. *J. Nat. Gas Chem.* **2008**, *17*, 288−292.
(12) Pan, Z.; Bukur, D. B. Fischer−Tropsch Synthesis on Co/ZnO Catalyst—Effect of Pretreatment Procedure. *Appl. Catal., A* **2011**, *404*, 74−80.
(13) Khodakov, A. Y.; Lynch, J.; Bazin, D.; Rebours, B.; Zanier, N.; Moisson, B.; Chaumette, P. Reducibility of Cobalt Species in Silica-Supported Fischer−Tropsch Catalysts. *J. Catal.* **1997**, *168*, 16−25.
(14) Lyu, S.; Wang, L.; Zhang, J.; Liu, C.; Sun, J.; Peng, B.; Wang, Y.; Rappé, K. G.; Zhang, Y.; Li, J.; Nie, L. Role of Active Phase in Fischer-Tropsch Synthesis: Experimental Evidence of CO Activation over Single-Phase Cobalt Catalysts. *ACS Catal.* **2018**, *8*, 7787−7798.
(15) Liu, J.-X.; Su, H.-Y.; Sun, D.-P.; Zhang, B.-Y.; Li, W.-X. Crystallographic Dependence of CO Activation on Cobalt Catalysts: HCP versus FCC. *J. Am. Chem. Soc.* **2013**, *135*, 16284−16287.
(16) Tsakoumis, N. E.; Patanou, E.; Lögdberg, S.; Johnsen, R. E.; Myrstad, R.; van Beek, W.; Rytter, E.; Blekkan, E. A. Structure−Performance Relationships on Co-Based Fischer−Tropsch Synthesis Catalysts: The More Defect-Free, the Better. *ACS Catal.* **2019**, *9*, 511−520.
(17) Paryjczak, T.; Rynkowski, J.; Karski, S. Thermoprogrammed Reduction of Cobalt Oxide Catalysts. *J. Chromatogr. A* **1980**, *188*, 254−256.
(18) Petersen, A. P.; Claeys, M.; Kooyman, P. J.; van Steen, E. Cobalt-Based Fischer−Tropsch Synthesis: A Kinetic Evaluation of Metal−Support Interactions Using an Inverse Model System. *Catalysts* **2019**, *9*, 794.
(19) Claeys, M.; Dry, M. E.; van Steen, E.; du Plessis, E.; van Berge, P. J.; Saib, A. M.; Moodley, D. J. In Situ Magnetometer Study on the Formation and Stability of Cobalt Carbide in Fischer−Tropsch Synthesis. *J. Catal.* **2014**, *318*, 193−202.
(20) Chase, M. W.; Curnutt, J. L.; Downey, J. R.; Mcdonald, R. A.; Syverud, A. N.; Valenzuela, E. A. JANAF Thermochemical Tables, 1982 Supplement. *J. Phys. Chem. Ref. Data* **1982**, *11*, 695−940.
(21) Paterson, J.; Peacock, M.; Ferguson, E.; Purves, R.; Ojeda, M. In Situ Diffraction of Fischer-Tropsch Catalysts: Cobalt Reduction and Carbide Formation. *ChemCatChem* **2017**, *9*, 3463−3469.
(22) Jacobs, G.; Ji, Y.; Davis, B. H.; Cronauer, D.; Kropf, A. J.; Marshall, C. L. Fischer−Tropsch Synthesis: Temperature Programmed EXAFS/XANES Investigation of the Influence of Support Type, Cobalt Loading, and Noble Metal Promoter Addition to the Reduction Behavior of Cobalt Oxide Particles. *Appl. Catal., A* **2007**, *333*, 177−191.
(23) Egerton, R. F. *Electron Energy-Loss Spectroscopy in the Electron Microscope*, 3rd ed.; Springer US: Boston, MA, 2011.
(24) Zhao, Y.; Feltes, T. E.; Regalbuto, J. R.; Meyer, R. J.; Klie, R. F. In Situ Electron Energy Loss Spectroscopy Study of Metallic Co and Co Oxides. *J. Appl. Phys.* **2010**, *108*, 063704.
(25) Pearson, D. H.; Ahn, C. C.; Fultz, B. White Lines and D-Electron Occupancies for the 3d and 4d Transition Metals. *Phys. Rev. B: Condens. Matter Mater. Phys.* **1993**, *47*, 8471−8478.
(26) Grunes, L. A.; Leapman, R. D.; Wilker, C. N.; Hoffmann, R.; Kunz, A. B. Oxygen K Near-Edge Fine Structure: An Electron-Energy-Loss Investigation with Comparisons to New Theory for Selected 3d Transition-Metal Oxides. *Phys. Rev. B: Condens. Matter Mater. Phys.* **1982**, *25*, 7157−7173.
(27) Suntivich, J.; Hong, W. T.; Lee, Y.-L.; Rondinelli, J. M.; Yang, W.; Goodenough, J. B.; Dabrowski, B.; Freeland, J. W.; Shao-Horn, Y. Estimating Hybridization of Transition Metal and Oxygen States in Perovskites from o k -Edge X-Ray Absorption Spectroscopy. *J. Phys. Chem. C* **2014**, *118*, 1856−1863.
(28) Brydson, R. *Aberration-Corrected Analytical Transmission Electron Microscopy*; Brydson, R., Ed.; John Wiley & Sons, Ltd: Chichester, UK, 2011.
(29) Braconnier, L.; Landrivon, E.; Clémençon, I.; Legens, C.; Diehl, F.; Schuurman, Y. How Does Activation Affect the Cobalt Crystallographic Structure? An in Situ XRD and Magnetic Study. *Catal. Today* **2013**, *215*, 18−23.
(30) Xin, H. L.; Pach, E. A.; Diaz, R. E.; Stach, E. A.; Salmeron, M.; Zheng, H. Revealing Correlation of Valence State with Nanoporous Structure in Cobalt Catalyst Nanoparticles by In Situ Environmental TEM. *ACS Nano* **2012**, *6*, 4241−4247.
(31) Wang, Z. L.; Yin, J. S.; Mo, W. D.; Zhang, Z. J. J. In-Situ Analysis of Valence Conversion in Transition Metal Oxides Using Electron Energy-Loss Spectroscopy. *J. Phys. Chem. B* **1997**, *101*, 6793−6798.
(32) Zhao, Y.; Feltes, T. E.; Regalbuto, J. R.; Meyer, R. J.; Klie, R. F. In-Situ Electron Energy Loss Spectroscopy Study of Mn-Promoted Co/TiO_2 Fischer−Tropsch Catalysts. *Catal. Lett.* **2011**, *141*, 641−648.
(33) Wang, Z. L.; Yin, J. S.; Jiang, Y. D. EELS Analysis of Cation Valence States and Oxygen Vacancies in Magnetic Oxides. *Micron* **2000**, *31*, 571−580.
(34) Ward, M. R.; Boyes, E. D.; Gai, P. L. In Situ Aberration-Corrected Environmental TEM: Reduction of Model Co_3O_4 in H_2 at the Atomic Level. *ChemCatChem* **2013**, *5*, 2655−2661.
(35) Dembélé, K.; Bahri, M.; Melinte, G.; Hirlimann, C.; Berliet, A.; Maury, S.; Gay, A.-S.; Ersen, O. Insight by In Situ Gas Electron Microscopy on the Thermal Behaviour and Surface Reactivity of Cobalt Nanoparticles. *ChemCatChem* **2018**, *10*, 4004−4009.
(36) Jacobs, G.; Das, T. K.; Zhang, Y.; Li, J.; Racoillet, G.; Davis, B. H. Fischer−Tropsch Synthesis: Support, Loading, and Promoter Effects on the Reducibility of Cobalt Catalysts. *Appl. Catal., A* **2002**, *233*, 263−281.
(37) Tauster, S. J.; Fung, S. C.; Baker, R. T. K.; Horsley, J. A. Strong Interactions in Supported-Metal Catalysts. *Science* **1981**, *211*, 1121−1125.
(38) den Breejen, J. P.; Radstake, P. B.; Bezemer, G. L.; Bitter, J. H.; Frøseth, V.; Holmen, A.; de Jong, K. P. On the Origin of the Cobalt Particle Size Effects in Fischer−Tropsch Catalysis. *J. Am. Chem. Soc.* **2009**, *131*, 7197−7203.
(39) Shi, N.; Cheng, W.; Zhou, H.; Fan, T.; Niederberger, M. Facile Synthesis of Monodisperse Co_3O_4 Quantum Dots with Efficient Oxygen Evolution Activity. *Chem. Commun.* **2015**, *51*, 1338−1340.
(40) Phaahlamohlaka, T. N.; Kumi, D. O.; Dlamini, M. W.; Forbes, R.; Jewell, L. L.; Billing, D. G.; Coville, N. J. Effects of Co and Ru Intimacy in Fischer-Tropsch Catalysts Using Hollow Carbon Sphere Supports: Assessment of the Hydrogen Spillover Processes. *ACS Catal.* **2017**, *7*, 1568−1578.
(41) Egerton, R. F. Inelastic Scattering of 80 KeV Electrons in Amorphous Carbon. *Philos. Mag.* **1975**, *31*, 199−215.
(42) Egerton, R. F. K-Shell Ionization Cross-Sections for Use in Microanalysis. *Ultramicroscopy* **1979**, *4*, 169−179.

https://doi.org/10.1021/acs.jpcc.2c00482
J. Phys. Chem. C 2022, 126, 6325−6333

(43) Johnson, D. W.; Spence, J. C. H. Determination of the Single-Scattering Probability Distribution from Plural-Scattering Data. *J. Phys. D: Appl. Phys.* **1974**, *7*, 771−780.
(44) Verbeeck, J.; Van Aert, S. Model Based Quantification of EELS Spectra. *Ultramicroscopy* **2004**, *101*, 207−224.
(45) Hofer, F. Determination of Inner-Shell Cross-Sections for EELS-Quantification. *Microsc., Microanal., Microstruct.* **1991**, *2*, 215−230.
(46) Leapman, R. D.; Rez, P.; Mayers, D. F. K, L, and M shell generalized oscillator strengths and ionization cross sections for fast electron collisions. *J. Chem. Phys.* **1980**, *72*, 1232−1243.
(47) Slater, T. *EPSIC-DLS/ParticleSpy: V0.4.1*; Zenodo, April 23, 2020.
(48) La Peña, F. D.; Prestat, E.; Fauske, V. T.; Burdet, P.; Jokubauskas, P.; Nord, M.; Furnival, T.; Ostasevicius, T.; MacArthur, K. E.; Johnstone, D. N.; et al. *Hyperspy/Hyperspy: HyperSpy 1.6.0*; Zenodo, August 5, 2020.
(49) Li, S.; Pasc, A.; Fierro, V.; Celzard, A. Hollow Carbon Spheres, Synthesis and Applications − a Review. *J. Mater. Chem. A* **2016**, *4*, 12686−12713.
(50) Bremmer, G. M.; Zacharaki, E.; Sjåstad, A. O.; Navarro, V.; Frenken, J. W. M.; Kooyman, P. J. In Situ TEM Observation of the Boudouard Reaction: Multi-Layered Graphene Formation from CO on Cobalt Nanoparticles at Atmospheric Pressure. *Faraday Discuss.* **2017**, *197*, 337−351.
(51) Nakamura, J.; Tanaka, K. ichi; Toyoshima, I. Reactivity of Deposited Carbon on $CoAl_2O_3$ Catalyst. *J. Catal.* **1987**, *108*, 55−62.
(52) Moodley, D. J.; van de Loosdrecht, J.; Saib, A. M.; Overett, M. J.; Datye, A. K.; Niemantsverdriet, J. W. Carbon Deposition as a Deactivation Mechanism of Cobalt-Based Fischer−Tropsch Synthesis Catalysts under Realistic Conditions. *Appl. Catal., A* **2009**, *354*, 102−110.
(53) Dai, Z. R.; Sun, S.; Wang, Z. L. Phase Transformation, Coalescence, and Twinning of Monodisperse FePt Nanocrystals. *Nano Lett.* **2001**, *1*, 443−447.
(54) Lyu, Z.; Chen, R.; Mavrikakis, M.; Xia, Y. Physical Transformations of Noble-Metal Nanocrystals upon Thermal Activation. *Acc. Chem. Res.* **2021**, *54*, 1−10.
(55) Wang, Z. L.; Bentley, J.; Evans, N. D. Valence State Mapping of Cobalt and Manganese Using Near-Edge Fine Structures. *Micron* **2000**, *31*, 355−362.
(56) Leapman, R. D.; Grunes, L. A. Anomalous L3L2 White-Line Ratios in the 3d Transition Metals. *Phys. Rev. Lett.* **1980**, *45*, 397−401.
(57) Gontard, L. C.; Dunin-Borkowski, R. E.; Gass, M. H.; Bleloch, A. L.; Ozkaya, D. Three-Dimensional Shapes and Structures of Lamellar-Twinned Fcc Nanoparticles Using ADF STEM. *J. Electron Microsc.* **2009**, *58*, 167−174.
(58) Clarebrough, L. M.; Forwood, C. T. Diffraction from Single and Overlapping Stacking Faults in F.C.C. Crystals. *Phys. Status Solidi A* **1976**, *33*, 355−366.
(59) Tang, C.; Shi, J.; Bai, X.; Hu, A.; Xuan, N.; Yue, Y.; Ye, T.; Liu, B.; Li, P.; Zhuang, P.; Shen, J.; Liu, Y.; Sun, Z. CO_2 Reduction on Copper's Twin Boundary. *ACS Catal.* **2020**, *10*, 2026−2032.
(60) Wilms, M.; Broekmann, P.; Kruft, M.; Stuhlmann, C.; Wandelt, K. STM Investigation of Step Orientation and Surface Dynamics of Cu(111) in Hydrochloric Acid Electrolyte. *Appl. Phys. A: Mater. Sci. Process.* **1998**, *66*, S473−S475.
(61) Kwak, G.; Kim, D.-E.; Kim, Y. T.; Park, H.-G.; Kang, S. C.; Ha, K.-S.; Jun, K.-W.; Lee, Y.-J. Enhanced Catalytic Activity of Cobalt Catalysts for Fischer−Tropsch Synthesis via Carburization and Hydrogenation and Its Application to Regeneration. *Catal. Sci. Technol.* **2016**, *6*, 4594−4600.
(62) Pei, Y.-P.; Liu, J.-X.; Zhao, Y.-H.; Ding, Y.-J.; Liu, T.; Dong, W.-D.; Zhu, H.-J.; Su, H.-Y.; Yan, L.; Li, J.-L.; Li, W.-X. High Alcohols Synthesis via Fischer−Tropsch Reaction at Cobalt Metal/Carbide Interface. *ACS Catal.* **2015**, *5*, 3620−3624.
(63) Moya-Cancino, J. G.; Honkanen, A.-P.; Van Der Eerden, A. M. J.; Oord, R.; Monai, M.; Ten Have, I.; Sahle, C. J.; Meirer, F.; Weckhuysen, B. M.; De Groot, F. M. F.; Huotari, S. In Situ X-Ray Raman Scattering Spectroscopy of the Formation of Cobalt Carbides in a Co/TiO_2 Fischer-Tropsch Synthesis Catalyst. *ACS Catal.* **2021**, *11*, 809−819.

https://doi.org/10.1021/acs.jpcc.2c00482
J. Phys. Chem. C 2022, 126, 6325−6333